Photodissociation of vibrationally excited SH and SD radicals at 288 and 291 nm: The S($^1D_2$) channel

Liesbeth M. C. Janssen, Mark P. J. van der Loo, and Gerrit C. Groenenboom
Theoretical Chemistry, Institute for Molecules and Materials (IMM), Radboud University Nijmegen, Toernooiveld 1, 6525 ED Nijmegen, The Netherlands

Shiou-Min Wu, Dragana Č. Radenović, André J. A. van Roij, Ivan Anton Garcia, and David H. Parker[a)]
Department of Molecular and Laser Physics, IMM, Radboud University Nijmegen, Toernooiveld 1, 6525 ED Nijmegen, The Netherlands

(Received 12 December 2006; accepted 18 January 2007; published online 6 March 2007)

Ultraviolet photodissociation of SH ($X\,^2\Pi$, $v''=2-7$) and SD ($X\,^2\Pi$, $v''=3-7$) has been studied at 288 and 291 nm, using the velocity map imaging technique to probe the angular and speed distributions of the S($^1D_2$) products. Photodissociation cross sections for the $A\,^2\Sigma^+ \leftarrow X\,^2\Pi(v'')$ and $^2\Delta \leftarrow X\,^2\Pi(v'')$ transitions have been obtained by *ab initio* calculations at the CASSCF-MRSDCI/aug-cc-pV5Z level of theory. Both the experimental and theoretical results show that SH/SD photodissociation from $X\,^2\Pi$ ($v'' \leqslant 7$) proceeds via the repulsive wall of the $A\,^2\Sigma^+$ state. The angular distributions of S($^1D_2$) indicate that the dissociation approaches the sudden recoil limit of the $A\,^2\Sigma^+$ state, yielding strongly polarized fragments. The S($^1D_2$) atoms are predominantly produced with total electronic angular momentum perpendicular to the recoil axis. © *2007 American Institute of Physics*. [DOI: 10.1063/1.2646522]

I. INTRODUCTION

The mercapto radical (SH) plays an important role in atmospheric chemistry, particularly in the oxidation of H_2S and various other sulfur-containing compounds.[1] SH is also a key intermediate in combustion processes of sulfur-containing fuels and has recently been observed in interstellar space.[2] The photochemistry of this radical is therefore of astrochemical importance.

The spectroscopy of the SH radical, and its isotopic analog SD, has been extensively studied over the last decades, both experimentally[3–11] and theoretically.[12–17] The electronic configuration of the $X\,^2\Pi$ ground state is $(1\sigma)^2(2\sigma)^2(3\sigma)^2(1\pi)^4(4\sigma)^2(5\sigma)^2(2\pi)^3$, thus SH and SD are open-shell systems. The first excited bound state, $A\,^2\Sigma^+$, is optically coupled to the ground $X\,^2\Pi$ state and correlates with H/D($^2S_{1/2}$)+S($^1D_2$) in the atomic limit. The $A\,^2\Sigma^+$ state is crossed by three repulsive curves ($^4\Sigma^-$, $1\,^2\Sigma^-$, and $^4\Pi$), which lead to the ground state products H/D($^2S_{1/2}$) and S(^3P_J). The repulsive $^4\Sigma^-$, $1\,^2\Sigma^-$, and $^4\Pi$ states are coupled to the bound $A\,^2\Sigma^+$ state via spin-orbit interactions, and the $A\,^2\Sigma^+$ state can therefore undergo predissociation through these repulsive curves. Numerous studies have investigated the predissociative character of the $A\,^2\Sigma^+$–$X\,^2\Pi$ system, and both radiative and predissociative lifetimes of SH/SD ($A\,^2\Sigma^+$, $v'=0-2$) have been determined.[13,17–22]

Above the dissociation threshold of the H/D($^2S_{1/2}$)+S($^1D_2$) channel, direct dissociation via the continuum region of the $A\,^2\Sigma^+$ state becomes possible. The S($^1D_2$) dissociation limit can also be reached by optical excitation to the higher repulsive $^2\Delta$ and $2\,^2\Pi$ states. The potential energy curves of the doublet states correlating with the S(^3P_J) and S($^1D_2$) atomic limits are shown in Fig. 1. Metastable S($^1D_2$) is more reactive than the S(^3P_J) ground state atom, and the S($^1D_2$) dissociation channel is therefore important in various chemical reactions, particularly in the astrochemical context. The oxygen analog O($^1D_2$) has already been observed in cometary matter and is primarily produced by OH photodissociation.[23] Based on the relatively high cosmic abundance of sulfur, it can be expected that S($^1D_2$) is also present in the interstellar medium, and photodissociation of SH might play an important role in the production process.

The direct dissociation channels of SH have been studied experimentally in the ultraviolet (UV) and vacuum-ultraviolet (VUV) region. Zhou *et al.*[24] studied the photodissociation dynamics of jet-cooled SH ($X\,^2\Pi$, $v'=0-2$) in the wavelength region of 216–232 nm and concluded that the UV photolysis of SH mainly proceeds via the repulsive $1\,^2\Sigma^-$ state. The observed S(^3P_J) fine structure state distribution indicated that the dissociation approaches the sudden recoil limit of the $1\,^2\Sigma^-$ state. However, they also noted that nonadiabatic interactions among the repulsive $^4\Sigma^-$, $1\,^2\Sigma^-$, and $^4\Pi$ states influence the final S(^3P_J) product distribution. No evidence was found for the H($^2S_{1/2}$)+S($^1D_2$) channel in this wavelength region, although the excitation energies are sufficiently high to reach the S($^1D_2$) limit. Continetti *et al.*[25] and Hsu *et al.*[26] investigated the secondary photodissociation of SH from photolysis of H_2S at 193 nm. They concluded that the observed S(^3P_J) and S($^1D_2$) products were most likely coming from direct dissociation through the repulsive $1\,^2\Sigma^-$ and $^2\Delta$ states, respectively. Chen *et al.*[27] recently studied the VUV photodissociation of jet-cooled SH at 121 nm and

[a)]Author to whom correspondence should be addressed. Electronic mail: parker@science.ru.nl

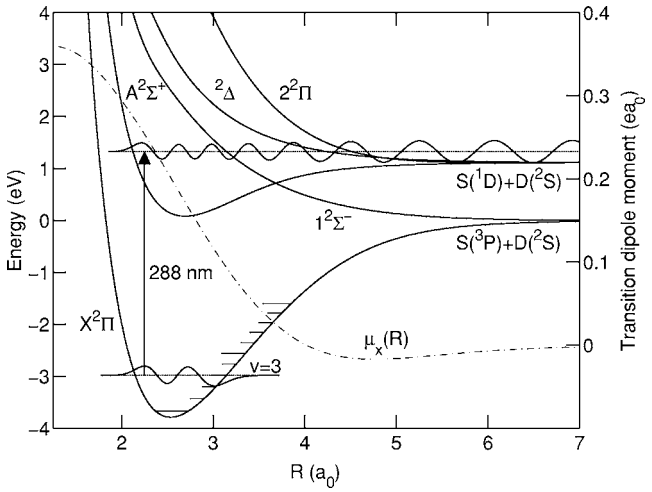

FIG. 1. Photodissociation of SD ($X\,^2\Pi$, $v''=3$) at 288 nm via the repulsive wall of the $A\,^2\Sigma^+$ state. The figure shows the calculated *ab initio* potentials, $A\,^2\Sigma^+ \leftarrow X\,^2\Pi$ transition dipole moment μ_x (ea_0), bound $X\,^2\Pi$ ($v''=3$) wave function, and continuum $A\,^2\Sigma^+$ wave function. The $1\,^2\Sigma^-$ and $2\,^2\Pi$ potentials are adapted from Ref. 17.

found that the $S(^3P_J)$ product fine structure distribution is significantly different from that in the UV region. They suggested that the minor $S(^3P_J)$ product originates from initial excitation to the $^2\Delta$ or $2\,^2\Pi$ state, which can couple nonadiabatically with other repulsive states to produce $S(^3P_J)$. The observed production of $S(^1D_2)$ was found to arise from the repulsive $2\,^2\Pi$ state. To our knowledge, no previous studies have detected $S(^1D_2)$ via the continuum of the $A\,^2\Sigma^+$ state.

Theoretical studies of the direct $S(^3P_J)$ and $S(^1D_2)$ photodissociation channels of SH have been conducted by Lee *et al.*[28,29] They predicted that the $S(^3P_J)$ and $S(^1D_2)$ vector properties show oscillatory variations due to interference among the different dissociation pathways. However, these findings seem to contradict the experimental results of Zhou *et al.*,[24] who reported that the $S(^3P_J)$ fine structure state distributions and anisotropy parameters are nearly constant in the energy range of 216–232 nm. Other theoretical work has mainly focused on the predissociative behavior of the $A\,^2\Sigma^+$ state, and accurate *ab initio* calculations on the direct dissociation channels of SH and SD are still limited in number.

This work aims to investigate the $S(^1D_2)$ photodissociation channel of vibrationally excited SH/SD radicals at 288 and 291 nm, both experimentally and theoretically. Measurements of the $S(^1D_2)$ product velocities are compared with cross sections for the $A\,^2\Sigma^+ \leftarrow X\,^2\Pi(v'')$ and $^2\Delta \leftarrow X\,^2\Pi(v')$ transitions in order to identify the dominant dissociation pathway. Additionally, the polarization of the sulfur fragments is studied to provide a complete description of the dissociation dynamics.

II. EXPERIMENT

The main concept of velocity map imaging[30] is to record a two-dimensional projection of nascent species in velocity space. The obtained image provides detailed information about the speed and angular distributions of the photodissociation products. The experimental setup has been described elsewhere,[31,32] and only a summary of the experimental details will be presented here.

A mixture of 25% D_2S seeded in Xe was expanded into a vacuum chamber through a pulsed Jordan valve (10 Hz), where the SD radicals were produced by a pulsed electrical discharge of $\approx$3 kV (10 μs pulse) at the beginning of the supersonic expansion. These discharge sources are known to produce rotationally cold but vibrationally excited species. Despite extensive flushing with D_2S, it was not possible to remove all H atoms from the surfaces of the gas handling system. For this reason, significant and varying amounts of SH were also formed in the discharge. The molecular beam was collimated by a 1 mm skimmer, after which the SH/SD molecules in the $X\,^2\Pi_{3/2}$, $J=3/2$, f lambda doublet state were focused using a 12 cm long hexapole with 6 mm diameter rods, operating at $\pm$10 kV. The molecular beam was then crossed with a linearly polarized laser to induce both photodissociation of the radicals and ionization of the S atoms. The laser beam was generated by a frequency doubled dye laser (Quanta-Ray PDL-2), pumped by a neodymium doped yttrium aluminum garnet laser (Quanta-Ray DCR-11, 10 Hz). The laser wavelength was tuned at either 288.19 or 291.48 nm, for (2+1) resonance enhanced multiphoton ionization (REMPI) detection of $S(^1D_2)$ products via $S(4p, ^1F_3)$ and $S(4p, ^1P_1)$, respectively. The pulse energy of the UV radiation was $\approx$2 mJ. Subsequently, the S^+ fragments were velocity mapped using an electrostatic lens, which consisted of a repeller, extractor, and ground electrode. The ions were projected onto a two-dimensional imaging detector consisting of two microchannel plates and a phosphor screen. The two-dimensional crushed image was recorded by a charge-coupled device camera (Pixelfly) and converted to a sliced image of the original three-dimensional distribution by applying an inverse Abel transformation.[33] All measurements were repeated several times.

III. CALCULATIONS

A. Photodissociation cross sections

In order to identify the pathway from which the observed $S(^1D_2)$ fragments arise, v''-dependent photodissociation cross sections were calculated for the $A\,^2\Sigma^+ \leftarrow X\,^2\Pi(v'')$ and $^2\Delta \leftarrow X\,^2\Pi(v'')$ transitions. The *ab initio* electronic wave functions and potential energy curves of the ground $X\,^2\Pi$ state and excited $A\,^2\Sigma^+$ and $^2\Delta$ states were calculated with the MOLPRO 2000 quantum chemistry package,[34] using the augmented correlation-consistent polarized valence quintuple-zeta (aug-cc-pV5Z) basis set.[35] The potentials were computed using the internally contracted multireference singles and doubles configuration interaction (MRS-DCI) method[36,37] including the Davidson correction.[38] The molecular orbitals were obtained from a complete active space self-consistent field (CASSCF) calculation,[39,40] where the three lowest σ orbitals and the first π_x and π_y orbitals were kept doubly occupied. The active space consisted of three σ orbitals, one π_x orbital, and one π_y orbital.

The electronic transition dipole moments of the $A\,^2\Sigma^+ \leftarrow X\,^2\Pi$ and $^2\Delta \leftarrow X\,^2\Pi$ transitions were calculated at the

MRSDCI level in MOLPRO, with the molecular orbitals taken from a state-averaged CASSCF calculation. The nuclear wave functions and vibrational energies of the bound $X\,^2\Pi$ and $A\,^2\Sigma^+$ states were obtained with the sinc-function discrete variable representation method,[41,42] using a grid in the range of $1-12a_0$ with a step size of $0.02a_0$. The continuum wave functions of the unbound region of the $A\,^2\Sigma^+$ state and the repulsive $^2\Delta$ state were computed on the same grid with the renormalized Numerov method.[43] The photodissociation cross sections of the $A\,^2\Sigma^+ \leftarrow X\,^2\Pi(v')$ and $^2\Delta \leftarrow X\,^2\Pi(v')$ transitions were then calculated using the relation[44]

$$\sigma(\omega) = \frac{4\pi^2 \alpha \hbar \omega}{3e^2} |\langle \Psi_f(E) | \mu_x(R) | X\,^2\Pi_x(v') \rangle|^2, \tag{1}$$

where $\hbar\omega$ is the energy of the absorbed photon, α the fine structure constant, e the elementary charge, $\Psi_f(E)$ the energy-normalized dissociative nuclear wave function at total energy E, and $\mu_x(R)$ the corresponding electronic transition dipole moment.

To evaluate the quality of the computed potentials, the $X\,^2\Pi$ vibrational frequencies of SH($v'=0-3$) and SD($v'=0-1$) have been compared to the experimental data from Ram *et al.*[10] and Pathak and Palmer,[5] respectively, and were found to be accurate within 0.5%. Experimental frequencies of the $A\,^2\Sigma^+$ state are more difficult to determine due to the occurrence of predissociation. Only the fundamental frequencies ($\Delta G_{1/2}$) have been reported for the $A\,^2\Sigma^+$ state of SH and SD,[4] which agree within 0.3% with the computed values. Moreover, the calculated bond dissociation energy D_0 of the SH ground $X\,^2\Pi$ state is 29 220 cm^{-1}, which is in excellent agreement with the recent experimental value of 29 245±25 cm^{-1} obtained by Zhou *et al.*[24] The computed energy difference between S(^3P) and S(^1D) was found to be 8912.69 cm^{-1}, which differs by 1.44% from the experimental data.[45] The potentials of the $A\,^2\Sigma^+$ and $^2\Delta$ states have therefore been slightly shifted vertically to match the experimental S(^3P)–S(^1D) splitting.

B. Fragment polarization

The polarization of S($^1D_2$) provides valuable insight into the photodissociation dynamics and can be interpreted using two different theoretical models. In the diabatic picture, the dissociation is assumed to be very fast with respect to the spin-orbit precession time, and the molecular wave function is projected directly onto the atomic states. Conversely, the adiabatic model assumes that the dissociation is much slower, and spin-orbit coupling must be taken into account. Both models are used in this study to calculate the S($^1D_2$) polarization arising from the $A\,^2\Sigma^+ \leftarrow X\,^2\Pi$ direct dissociation channel, which is expected to be dominant in the UV region. The results allow a qualitative analysis of the observed S($^1D_2$) alignment.

Experimentally, the polarization of the S($^1D_2$) fragments is reflected in the angular distribution of the velocity map images. The observed ion distribution is the product of the photofragment angular recoil distribution and the ionization efficiency and can be written as an expansion of ordinary Legendre polynomials P_l,[46,47]

$$I_{\text{ion}}(\theta) \propto \sum_{l=0,2,4,6} c_l P_l(\cos\theta), \tag{2}$$

where θ is the recoil angle with respect to the polarization axis of the laser. In the case of a purely perpendicular transition, for which the anisotropy parameter β equals -1, the expansion coefficients are given by:[47,48]

$$\begin{aligned} c_0 &= 1 - \frac{1}{5}\frac{\rho_0^{(2)}}{\rho_0^{(0)}} I_2, \\ c_2 &= \frac{5}{7}\frac{\rho_0^{(2)}}{\rho_0^{(0)}} I_2 - \frac{2}{7}\frac{\rho_0^{(4)}}{\rho_0^{(0)}} I_4 - 1, \\ c_4 &= -\frac{18}{35}\frac{\rho_0^{(2)}}{\rho_0^{(0)}} I_2 + \frac{57}{77}\frac{\rho_0^{(4)}}{\rho_0^{(0)}} I_4, \\ c_6 &= -\frac{5}{11}\frac{\rho_0^{(4)}}{\rho_0^{(0)}} I_4, \end{aligned} \tag{3}$$

where I_k are the relative geometrical factors of the ionization scheme and $\rho_0^{(k)}$ are the irreducible components of the density matrix (state multipoles) for the sulfur atom in the body-fixed frame. The factors I_k can be calculated using the theory by Mo *et al.*[46,49] It follows that $I_0:I_2:I_4 = 1:4\sqrt{70}/49:-3\sqrt{14}/98$ for the REMPI scheme via S($^1F_3$) at 288 nm and $I_0:I_2:I_4 = 1:-\sqrt{70}/14:-2\sqrt{14}/7$ for the S($^1P_1$) resonance at 291 nm. The state multipoles $\rho_0^{(k)}$ can be obtained using Eq. (24) of Ref. 47,

$$\rho_0^{(k)} = \sum_{\Omega_S} (-1)^{J_S - \Omega_S} \langle J_S, \Omega_S; J_S, -\Omega_S | k, 0 \rangle \rho_{\Omega_S;\Omega_S}, \tag{4}$$

where the symbol $\langle J_S, \Omega_S; J_S, -\Omega_S | k, 0 \rangle$ is a Clebsch-Gordan coefficient. The quantum number Ω_S denotes the projection of the total angular momentum of the sulfur atom $J_S=2$ with respect to the internuclear (recoil) axis. The term $\rho_{\Omega_S;\Omega_S}$ represents the Ω_S state populations, i.e., the diagonal elements of the density matrix for sulfur. Note that the off-diagonal elements of this density matrix are not taken into account, which is a direct consequence of ignoring the possible effects of coherent excitation. The populations in the different Ω_S states effectively determine the polarization of the S($^1D_2$) atom, and it is thus necessary to evaluate the density matrix explicitly. In this study, both the diabatic and adiabatic models are employed to predict which Ω_S states are populated.

In the diabatic model, the molecular $A\,^2\Sigma^+$ state is described by the Hunds case (a) electronic quantum numbers Λ, S, and Σ, denoting the body-fixed electronic orbital angular momentum projection, total electronic spin, and spin projection, respectively. The atomic fragments are described by the corresponding atomic quantum numbers Λ_i, S_i, and Σ_i, where i labels the particular atom. The quantum numbers L_i refer to the orbital angular momentum of the atoms. As spin-orbit recoupling is neglected in this model, $\Lambda = \Lambda_S + \Lambda_H$ is conserved during the photodissociation process. Given that $\Lambda=0$ for the $A\,^2\Sigma^+$ state and $\Lambda_H=0$ for the H($^2S_{1/2}$) atom, it follows that the S($^1D_2$) fragment is produced in the $\Lambda_S = \Omega_S = 0$ state. This reduces the summation in Eq. (4) to a single term, and the expansion coefficients c_l can be readily

TABLE I. Simulation parameters for the TKER and angular distributions of the $S(^1D_2)$ velocity map images, obtained at 288 and 291 nm using REMPI detection via $S(^1F_3)$ and $S(^1P_1)$, respectively. The parameter T denotes the vibrational temperature, SH/SD is the total signal ratio between SH and SD, Δv is the velocity resolution, and $\tilde{c}_l$ are the normalized Legendre moments. The calculated Legendre moments for the diabatic and adiabatic models are also given.

		T (K)	SH/SD	Δv (m/s)	$\tilde{c}_2$	$\tilde{c}_4$	$\tilde{c}_6$
$S(^1F_3) \leftarrow S(^1D_2)$	Image (a)	2300	1.7	35	−0.96	0.10	0.08
	Image (b)	2700	1.4	43	−0.92	0.13	0.02
	Diabatic	⋯	⋯	⋯	−1.32	0.24	0.07
	Adiabatic	⋯	⋯	⋯	−1.23	0.28	−0.05
$S(^1P_1) \leftarrow S(^1D_2)$	Image (c)	2500	1.2	38	0.24	−1.38	0.46
	Image (d)	2200	0.2	35	−0.48	−1.04	0.64
	Diabatic	⋯	⋯	⋯	0	−1.91	0.91
	Adiabatic	⋯	⋯	⋯	−1.15	0.71	−0.56

obtained from Eq. (3). To compare these results with the experimental data, the expansion coefficients are expressed in terms of normalized Legendre moments $\tilde{c}_l = c_l / c_0$.[47,48] The values of $\tilde{c}_l$ are given in Table I for both detection schemes.

In the spin-orbit adiabatic limit, $\Omega = \Lambda + \Sigma$ is assumed to be conserved during dissociation. The $A\ ^2\Sigma^+$ state is labeled by the quantum number $|\Omega| = 1/2$ and correlates to $|\Omega_S \Omega_H\rangle$ in the long range. The higher lying $2\ ^2\Pi$ state also has an $|\Omega| = 1/2$ fine structure component but correlates to a different $|\Omega_S \Omega_H\rangle$ state. In order to construct the adiabatic correlation diagram, the energy ordering of the $|\Omega_S \Omega_H\rangle = |0, 1/2\rangle$ and $|1, -1/2\rangle$ states must be evaluated at long range. As the spin-orbit interaction is zero for both atoms, we assume that spin-orbit coupling is negligible at large internuclear distances. Moreover, the long range quadrupole-quadrupole interaction is zero, since the hydrogen atom is produced in an S state. Consequently, the leading term that lifts the degeneracy of the $|\Omega_S \Omega_H\rangle$ states is the dispersion interaction. This is also the case in, e.g., the $He(^1S) - Sc(^2D)$ system, which has been worked out explicitly by Chu *et al.*[50] Following their notation, the dispersion interaction between $H(^2S_{1/2})$ and $S(^1D_2)$ as a function of the internuclear distance R is written as

$$V_\Lambda(R) \simeq -\frac{C_6(L,\Lambda)}{R^6}, \tag{5}$$

where $L = L_S = 2$. The quantum number $\Lambda = \Lambda_S = 0$ corresponds to the $|\Omega_S = 0, \Omega_H = 1/2\rangle$ state and $\Lambda = \Lambda_S = 1$ to the $|\Omega_S = 1, \Omega_H = -1/2\rangle$ state. Hence, we must determine the energy ordering of the Born-Oppenheimer potentials $V_0(R) = V_\Sigma(R)$ and $V_1(R) = V_\Pi(R)$ at long range. The dispersion coefficients $C_6(L,\Lambda)$ are given by

$$C_6(L,\Lambda) = C_{6,0}(L) - \frac{3\Lambda^2 - L(L+1)}{(2L-1)(2L+3)} C_{6,2}(L), \tag{6}$$

where $C_{6,0}(L)$ and $C_{6,2}(L)$ denote the scalar and (rank 2) tensor components of the dispersion interaction, respectively. From this equation, it follows that the energy ordering of the Λ states is determined by $\Lambda^2 C_{6,2}(L)$. The sign of $C_{6,2}(L)$ can be evaluated using the following expression:[50]

$$C_{6,2}(L) = -\frac{3(2L+3)}{2\pi L} \int_0^\infty \alpha_2(L; i\omega) \bar{\alpha}_H(i\omega) d\omega, \tag{7}$$

where $\alpha_2(L; i\omega)$ is the tensor polarizability of the $S(^1D_2)$ atom at imaginary frequency $i\omega$ and $\bar{\alpha}_H(i\omega)$ is the dynamic polarizability of the $H(^2S_{1/2})$ atom. The factor $\bar{\alpha}_H(i\omega)$ is positive for all angular frequencies ω (Ref. 51) and takes its maximum value at $\omega = 0$. Although we did not find $\alpha_2(L; i\omega)$ in the literature, we assume that the sign of the integral is determined by the sign at $\omega = 0$, which also holds for the $He(^1S) - Sc(^2D)$ and $He(^1S) - Ti(^3F)$ systems.[50] The sign of $\alpha_2(L) = \alpha_2(L, \omega = 0)$ can be derived using Eq. (11) of Ref. 50, where the polarizability anisotropy $\Delta\alpha(L, \Lambda; i\omega)$ is defined. In the case of $\Lambda = 0$ and $\omega = 0$, this equation may be rewritten as

$$\alpha_2(L) = -\frac{2}{3} \Delta\alpha(L,0) \frac{L(2L-1)}{L(L+1)}. \tag{8}$$

The quantity $\Delta\alpha(L,0)$ has been calculated by Medved *et al.*,[52] who reported a negative value of −6.43 a.u. for $S(^1D_2)$. Consequently, the tensor polarizability $\alpha_2(L)$ is positive, $C_{6,2}(L)$ is negative, and the total dispersion interaction depends linearly on $-\Lambda^2$. The energy ordering in the long range is thus given by $V_2(R) < V_1(R) < V_0(R)$, which leads to the

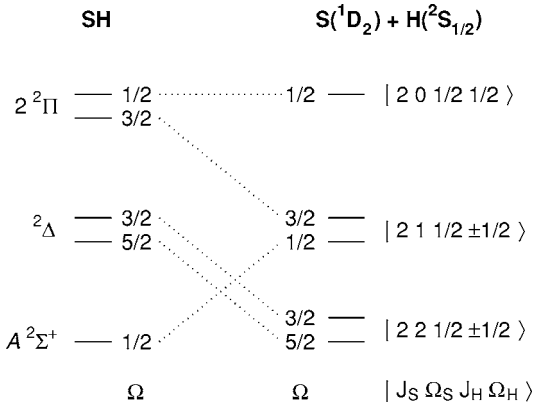

FIG. 2. Adiabatic correlation diagram for the $S(^1D_2) + H(^2S_{1/2})$ photodissociation channel of SH. The quantum number Ω denotes the projection of the total electronic angular momentum with respect to the internuclear axis and correlates to $\Omega_S + \Omega_H$ in the long range.

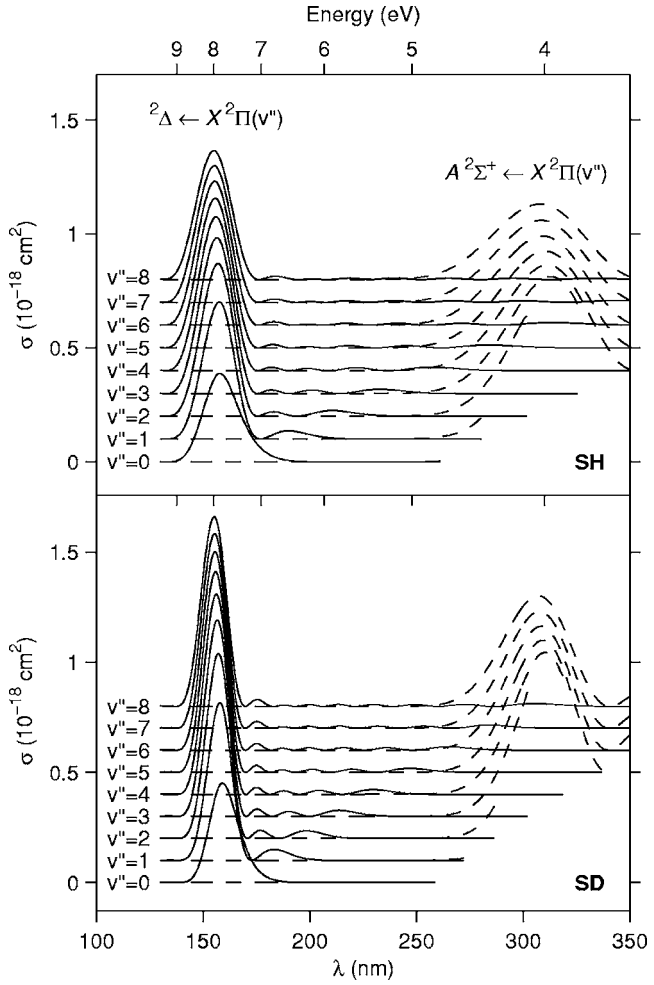

FIG. 3. Calculated v''-dependent SH/SD photodissociation cross sections for the S($^1D_2$) channel in the wavelength region of 130–350 nm. The dashed lines correspond to the $A\,^2\Sigma^+ \leftarrow X\,^2\Pi(v'')$ transition and the solid lines to the $^2\Delta \leftarrow X\,^2\Pi(v'')$ transition. The cross sections for $X\,^2\Pi(v''=1-8)$ are each plotted with an offset of 0.1×10^{-18} cm^2 for clarity.

correlation diagram shown in Fig. 2. Note that the energy ordering of the molecular $A\,^2\Sigma^+$, $2\,^2\Pi$, and $^2\Delta$ states is based on the ordering in the Franck-Condon region.

Figure 2 shows that the $A\,^2\Sigma^+$ state correlates adiabatically with the $|\Omega_S|=1$ component of S($^1D_2$), whereas the diabatic model predicts $\Omega_S=0$. The normalized Legendre moments for the adiabatic limit are given in Table I.

IV. RESULTS AND DISCUSSION

Figure 1 illustrates the photodissociation of SD ($X\,^2\Pi$, $v''=3$) at 288 nm based on the computed potentials and wave functions. The largest Franck-Condon overlap between the ground state and the continuum region of the $A\,^2\Sigma^+$ state is found at the inner wall of the potential. The repulsive $^2\Delta$ state is hardly accessible at this wavelength.

A. Photodissociation cross sections

The photodissociation cross sections of SH/SD for the $A\,^2\Sigma^+ \leftarrow X\,^2\Pi(v'')$ and $^2\Delta \leftarrow X\,^2\Pi(v'')$ transitions, both yielding S($^1D_2$), are presented in Fig. 3. Numerical values are available from the authors upon request. It can be seen that

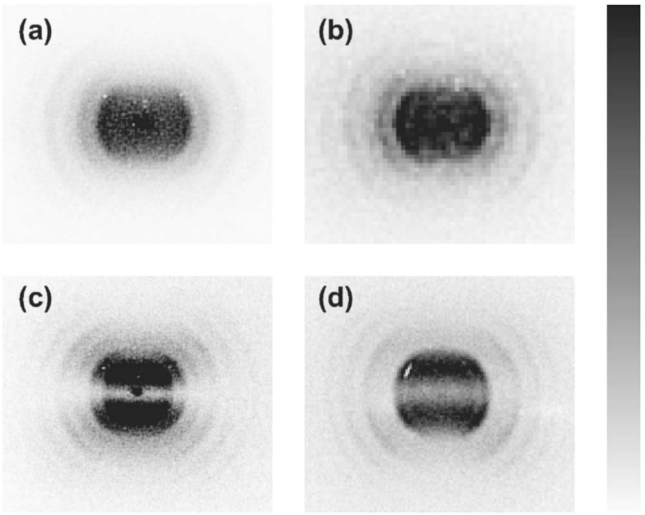

FIG. 4. Raw velocity map images of S($^1D_2$) from SH/SD photodissociation at [(a) and (b)] 288 nm and [(c) and (d)] 291 nm. The S($^1D_2$) fragments were detected by (2+1) REMPI via S($^1F_3$) and S($^1P_1$), respectively. The signal intensity is indicated in a gray scale, where the darkest area corresponds to the highest signal. The laser polarization is along the vertical axis in the figure.

the width of the cross section peaks is significantly larger for SH than for SD. This broadening can be qualitatively understood based on the reflection principle, as the vibrational states of SH are more delocalized than the states of SD.

At the S($^1D_2$) REMPI wavelengths of 288 and 291 nm, it is evident from Fig. 3 that S($^1D_2$) can only be produced by direct dissociation of vibrationally excited SH/SD via the repulsive part of the $A\,^2\Sigma^+$ state, whereas the $^2\Delta \leftarrow X\,^2\Pi$ transition is dominant in the VUV region. It is expected that the $2\,^2\Pi$ state becomes important at even higher energies. Note that the excitation wavelengths of 288 and 291 nm are insufficient to produce S($^1D_2$) from SH ($X\,^2\Pi$, $v''=0-1$) and SD ($X\,^2\Pi$, $v''=0-2$). The photodissociation cross sections are consistent with the work of Continetti *et al.*[25] and Hsu *et al.*,[26] who both reported that the S($^1D_2$)+H($^2S_{1/2}$) dissociation channel at 193 nm proceeds via the $^2\Delta$ state. The recent work of Chen *et al.*[27] showed that the S($^1D_2$) product of SH photodissociation at 121 nm mainly arises from the repulsive $2\,^2\Pi$ state rather than the $^2\Delta$ state. Given that the computed cross sections for the $^2\Delta \leftarrow X\,^2\Pi$ transition are nearly zero at this high energy, the $2\,^2\Pi$ state is thus expected to be dominant. In the UV region of 216–232 nm, Zhou *et al.*[24] found no evidence for the S($^1D_2$)+H($^2S_{1/2}$) dissociation channel of SH($v''=0-2$), which is also consistent with the calculated cross sections. In this wavelength region, the cross sections for both the $A\,^2\Sigma^+ \leftarrow X\,^2\Pi$ and $^2\Delta \leftarrow X\,^2\Pi$ transitions are negligible for the lowest vibrational states.

B. TKER distributions

The experimental S^+ velocity map images are shown in Fig. 4. The central spots in images 4(a)–4(c) originate from S($^1D_2$) produced directly by the electrical discharge, yielding fragments with zero velocity in the plane of the detector. Image 4(d) was obtained under slightly different experimental conditions, producing less S($^1D_2$) in the discharge. The

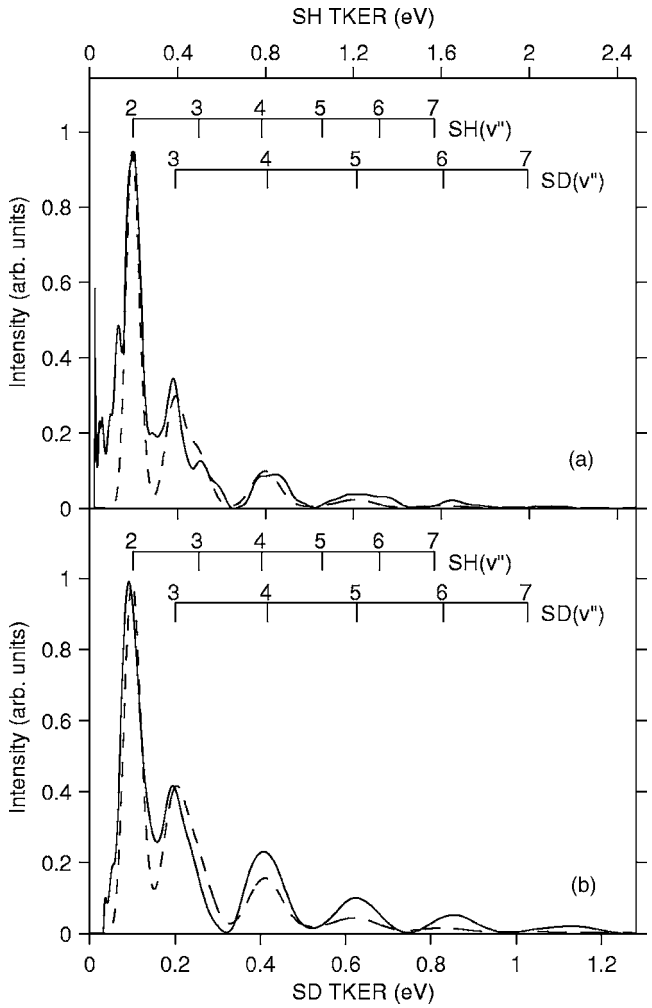

FIG. 5. Total kinetic energy release (TKER) distributions of SH/SD photodissociation at 288 nm derived from the corresponding $S(^1D_2)$ velocity map images in Figs. 4(a) and 4(b). The experimental data are plotted as solid lines and the simulated TKER distributions as dashed lines. The simulation parameters are given in Table I (see Sec. IV B for details).

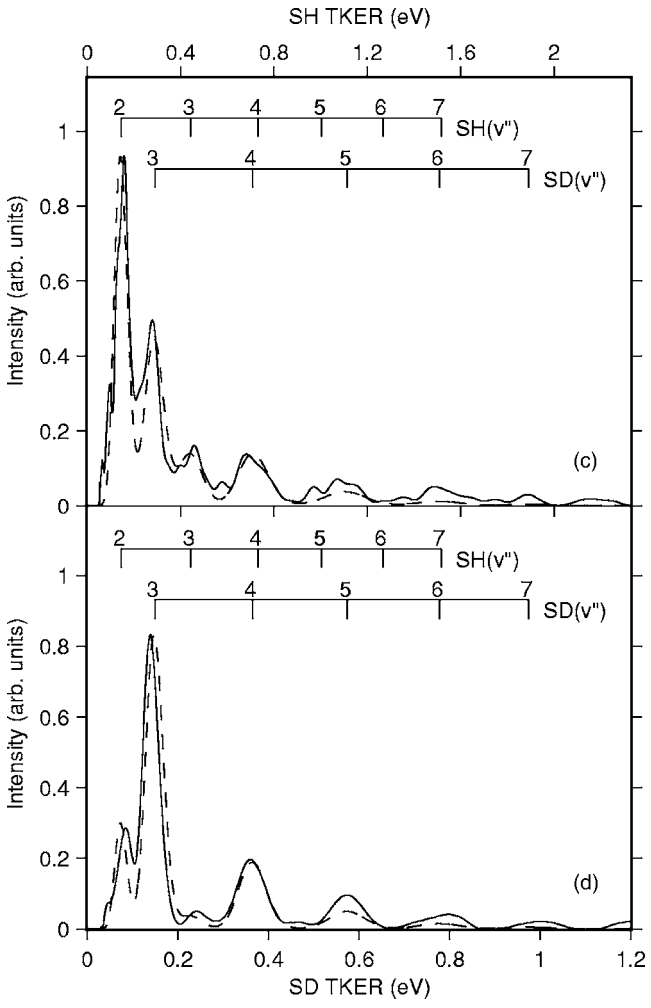

FIG. 6. Total kinetic energy release (TKER) distributions of SH/SD photodissociation at 291 nm derived from the corresponding $S(^1D_2)$ velocity map images in Figs. 4(c) and 4(d). The experimental data are plotted as solid lines and the simulated TKER curves as dashed lines. The simulation parameters are given in Table I (see Sec. IV B for details).

outer rings in the images arise from $S(^1D_2)$ fragments with higher velocities, corresponding to different vibrationally excited SH/SD $X\,^2\Pi$ molecules. The images are calibrated using the $S(^1D_2)$ signal from two-photon photodissociation of S_2 at 291 nm, where also S_2 is formed in the discharge.

The S^+ speed distributions of the images, obtained from integrating over the angular distributions, can be converted to total kinetic energy release: $\mathrm{TKER_{SH}}=(m_{\mathrm{SH}}/m_{\mathrm{H}})\times\mathrm{KER_S}$, $\mathrm{TKER_{SD}}=(m_{\mathrm{SD}}/m_{\mathrm{D}})\times\mathrm{KER_S}$. Background-subtracted TKER curves are presented in Figs. 5 and 6. Each peak in the TKER distribution is assigned to a different initial vibrational level of SH or SD, using the energy balance equation:

$$\mathrm{TKER}=h\nu+E_{\mathrm{int}}-D_0-E_{\mathrm{S}(^1D)}, \tag{9}$$

where $h\nu$ is the photon energy, E_{int} the internal vibrational energy of SH/SD, D_0 the bond energy with respect to the atomic $\mathrm{H/D}(^2S_{1/2})+\mathrm{S}(^3P)$ fragments, and $E_{\mathrm{S}(^1D)}$ the energy difference between $S(^3P)$ and $S(^1D)$.

The relative intensities of the peaks in the TKER distributions can be compared to the computed cross sections for each vibrational state. As the total signal intensity is a product of the cross sections and the population of each vibrational level, the initial ground state populations of SH and SD can be derived from the obtained data. Additionally, the experimental resolution can be determined by evaluating the width of the observed peaks. The dashed curves in Figs. 5 and 6 are the simulated TKER distributions based on the $A\,^2\Sigma^+\leftarrow X\,^2\Pi(v')$ cross sections. The curves are obtained as a function of the vibrational temperature (T), SH/SD signal intensity ratio, and peak width (Δv). The vibrational temperature is based on a Maxwell-Boltzmann distribution and is assumed to be the same for both SH and SD in each image. The peak width is obtained from the corresponding speed distributions, where the peaks are assumed to be Gaussian shaped with a constant full width at half maximum (FWHM) in each distribution. The simulation parameters are given in Table I. It can be seen that vibrational temperatures in the range of 2100–2700 K allow a reasonable simulation of the observed TKER distributions. The experimental velocity resolution Δv varies from 35 to 43 m/s (FWHM), which is mainly caused by the ion-electron recoil in the (2+1) REMPI process. These findings are consistent with the work of Radenović *et al.*,[31,53] who estimated a vibrational tempera-

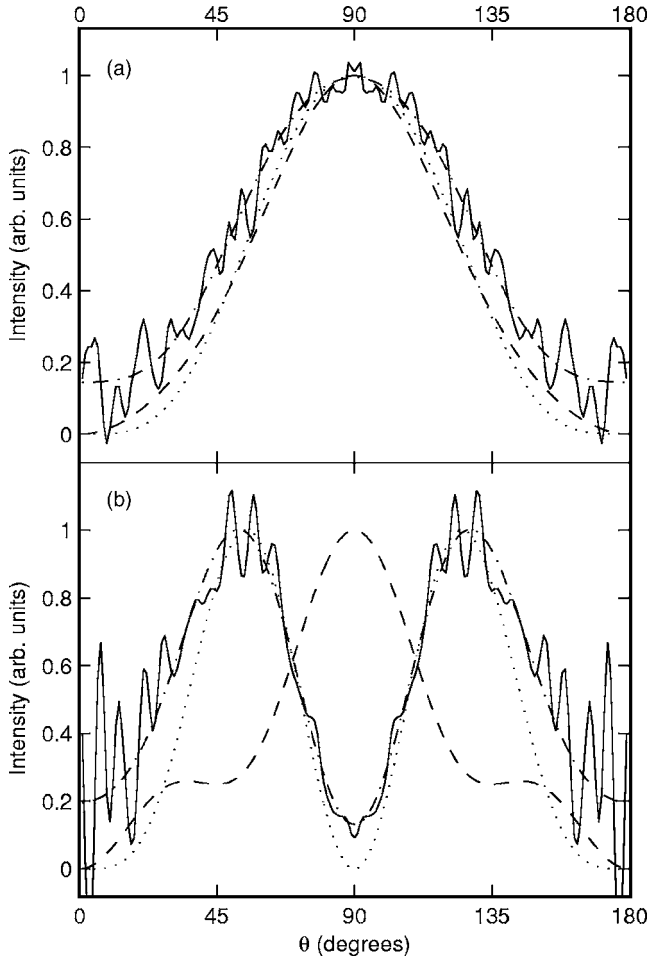

FIG. 7. Ion angular distributions obtained at (a) 288 nm using the S($^1F_3$) ← S($^1D_2$) REMPI scheme and (b) 291 nm using the S($^1P_1$) ← S($^1D_2$) REMPI scheme. The angular distributions are derived from the velocity map images in Figs. 4(a) and 4(c), respectively. The experimental data are plotted as solid lines and the fitted curves as dash-dotted lines. The fit parameters are listed in Table I. The dotted and dashed lines indicate the results for the diabatic and adiabatic models, respectively.

ture of 1700–2000 K for OD using the same experimental setup and an uncertainty of ±25 m/s in the oxygen atom velocities. Furthermore, Table I indicates different SH/SD signal ratios for each TKER distribution. Reducing the SH signal would require extra treatment of the gas line and nozzle. Nevertheless, measuring the signal from both SH and SD provides extra information within a single image.

C. Angular distributions

The angular distributions of the Abel-inverted S($^1D_2$) velocity map images are fitted to Legendre polynomials, as expressed in Eq. (2). The experimental distributions and fits are shown in Fig. 7. These curves are derived from images 4(a) and 4(c), obtained at 288 and 291 nm, respectively. Images 4(b) and 4(d) yield similar angular distributions but contain more background signal. The fitted Legendre moments of the ion images are listed in Table I. The experimental curves shown in Fig. 7 represent the angular distributions of the strongest rings in the images, with the best signal-to-noise ratio. Angular distributions at different kinetic energies are identical within the experimental noise, i.e., the curves are independent of v''. The difference between the signal arising from SH(v'') and SD(v'') is also insignificant.

The dotted and dashed lines in Fig. 7 indicate the results for the diabatic and adiabatic limits of the $A\,^2\Sigma^+$ state, respectively. The corresponding moments $\tilde{c}_l$ are given in Table I. Although both calculations agree well with the experimental data at 288 nm, the results at 291 nm show a clear distinction between the two models. It can be seen in Fig. 7(b) that the diabatic model ($\Omega_S=0$) reproduces the angular distribution at 291 nm very accurately, whereas the adiabatic model ($\Omega_S=1$) is in poor agreement with the experimental data. The deviation from the diabatic limit could be caused by the background signal, which leads to more isotropic distributions. The largest deviations are found in the regions around 0° and 180°, where the signal is very weak and the Abel inversion noise is large. Consequently, the poor signal-to-noise ratio causes relatively large errors. These findings, and the observation that the angular distributions are independent of v', unambiguously establish that the photodissociation approaches the sudden recoil limit of the $A\,^2\Sigma^+$ state. The S($^1D_2$) fragments are thus dominantly produced in the $\Omega_S=0$ level, where the total angular momentum J_S is perpendicular to the recoil axis. Such strongly polarized atoms could be relevant in various reactive collision experiments, in particular, to study the role of vector correlations.[54] Moreover, it should be noted that other sources of atomic sulfur, e.g., UV photolysis of OCS, yield S($^1D_2$) in all possible Ω_S states.[46,55] It is therefore remarkable that UV photodissociation of SH and SD induces such purely aligned fragments in the $\Omega_S=0$ state.

V. CONCLUSIONS

The photodissociation of vibrationally excited SH and SD radicals has been studied at the S($^1D_2$) REMPI wavelengths of 288 and 291 nm, using the experimental velocity map imaging technique to measure the speed and angular distributions. The radicals were produced by an electrical discharge source, yielding vibrational temperatures of ~2400 K. Both the experimental results and complementary *ab initio* calculations indicate that the S($^1D_2$) photodissociation channel proceeds via the $A\,^2\Sigma^+ \leftarrow X\,^2\Pi$ transition. The repulsive $^2\Delta$ state is predicted to become important at higher excitation energies. The observed alignment of S($^1D_2$) is consistent with the sudden recoil limit of the $A\,^2\Sigma^+$ state, where the S($^1D_2$) fragments are strongly polarized and predominantly produced in the $\Omega_S=0$ level. The total electronic angular momentum of the sulfur atom is thus perpendicular to the recoil axis.

ACKNOWLEDGMENTS

The authors gratefully acknowledge support for the experimental work from the Dutch National Science Foundation (FOM-MAPII) and from the EU network PICNIC. The *ab initio* work has been financially supported by the Council for Chemical Sciences of the Netherlands Organization for Scientific Research (CW-NWO). The authors also thank Professor Ad van der Avoird for carefully reading the manuscript.

[1] R. P. Wayne, *Chemistry of Atmospheres* (Oxford University Press, Oxford, 2000).
[2] I. Yamamura, K. Kawaguchi, and S. T. Ridgway, Astrophys. J. **528**, L33 (2000).
[3] D. A. Ramsay, J. Chem. Phys. **20**, 1920 (1952).
[4] J. W. C. Johns and D. A. Ramsay, Can. J. Phys. **39**, 210 (1961).
[5] C. M. Pathak and H. B. Palmer, J. Mol. Spectrosc. **32**, 157 (1969).
[6] W. L. Meerts and A. Dymanus, Can. J. Phys. **53**, 2123 (1975).
[7] J. J. Tiee, F. B. Wampler, R. C. Oldenborg, and W. W. Rice, Chem. Phys. Lett. **82**, 80 (1981).
[8] L. Schnieder, W. Meier, K. H. Welge, M. N. R. Ashfold, and C. M. Western, J. Chem. Phys. **92**, 7027 (1990).
[9] S. H. Ashworth and J. M. Brown, J. Mol. Spectrosc. **153**, 41 (1992).
[10] R. S. Ram, P. F. Bernath, R. Engleman, Jr., and J. W. Brault, J. Mol. Spectrosc. **172**, 34 (1995).
[11] E. Klisch, T. Klaus, S. P. Belov, A. Dolgner, R. Schieder, G. Winnewisser, and E. Herbst, Astrophys. J. **473**, 1118 (1996).
[12] D. M. Hirst and M. F. Guest, Mol. Phys. **46**, 427 (1982).
[13] L. Senekowitsch, H.-J. Werner, P. Rosmus, E.-A. Reinsch, and S. V. ONeil, J. Chem. Phys. **83**, 4661 (1985).
[14] P. J. Bruna and G. Hirsch, Mol. Phys. **61**, 1359 (1987).
[15] J. K. Park and H. Sun, Chem. Phys. Lett. **194**, 485 (1992).
[16] M. R. Manaa, Int. J. Quantum Chem., Quantum Chem. Symp. **29**, 577 (1995).
[17] S. M. Resende and F. R. Ornellas, J. Chem. Phys. **115**, 2178 (2001).
[18] J. J. Tiee, M. J. Ferris, and F. B. Wampler, J. Chem. Phys. **79**, 130 (1983).
[19] M. D. Wheeler, A. J. Orr-Ewing, and M. N. R. Ashfold, J. Chem. Phys. **107**, 7591 (1997).
[20] R. R. Friedl, W. H. Brune, and J. G. Anderson, J. Chem. Phys. **79**, 4227 (1983).
[21] W. Ubachs, J. J. ter Meulen, and A. Dymanus, Chem. Phys. Lett. **101**, 1 (1983).
[22] G. W. Loge and J. J. Tiee, J. Chem. Phys. **89**, 7167 (1988).
[23] J. P. Morgenthaler, W. M. Harris, F. Scherb, C. M. Anderson, R. J. Oliversen, N. E. Doane, M. R. Combi, M. L. Marconi, and W. H. Smyth, Astrophys. J. **563**, 451 (2001).
[24] W. Zhou, Y. Yuan, S. Chen, and J. Zhang, J. Chem. Phys. **123**, 054330 (2005).
[25] R. E. Continetti, B. A. Balko, and Y. T. Lee, Chem. Phys. Lett. **182**, 400 (1991).
[26] C.-W. Hsu, C.-L. Liao, Z.-X. Ma, P. J. H. Tjossem, and C. Y. Ng, Chem. Phys. Lett. **199**, 78 (1992).
[27] S. Chen, W. Zhou, and J. Zhang, Chem. Phys. Lett. **418**, 328 (2006).
[28] S. Lee, H. Sun, B. Kim, and K. F. Freed, J. Chem. Phys. **114**, 5537 (2001).
[29] S. Lee, H. Sun, B. Kim, and K. F. Freed, J. Chem. Phys. **116**, 10656 (2002).
[30] A. T. J. B. Eppink and D. H. Parker, Rev. Sci. Instrum. **68**, 3477 (1997).
[31] D. Č. Radenović, A. J. A. van Roij, D. A. Chestakov, A. T. J. B. Eppink, J. J. ter Meulen, D. H. Parker, M. P. J. van der Loo, G. C. Groenenboom, M. E. Greenslade, and M. I. Lester, J. Chem. Phys. **119**, 9341 (2003).
[32] M. E. Greenslade, M. I. Lester, D. Č. Radenović, A. J. A. van Roij, and D. H. Parker, J. Chem. Phys. **123**, 074309 (2005).
[33] V. Dribinski, A. Ossadtchi, V. A. Mandelshtam, and H. Reisler, Rev. Sci. Instrum. **73**, 2634 (2002).
[34] H.-J. Werner, P. J. Knowles, R. D. Amos *et al.*, MOLPRO is a package of *ab initio* programs.
[35] D. E. Woon and T. H. Dunning, Jr., J. Chem. Phys. **98**, 1358 (1993).
[36] H.-J. Werner and P. J. Knowles, J. Chem. Phys. **89**, 5803 (1988).
[37] P. J. Knowles and H.-J. Werner, Chem. Phys. Lett. **145**, 514 (1988).
[38] S. R. Langhoff and E. R. Davidson, Int. J. Quantum Chem. **8**, 61 (1974).
[39] H.-J. Werner and P. J. Knowles, J. Chem. Phys. **82**, 5053 (1985).
[40] P. J. Knowles and H.-J. Werner, Chem. Phys. Lett. **115**, 259 (1985).
[41] G. C. Groenenboom and D. T. Colbert, J. Chem. Phys. **99**, 9681 (1993).
[42] D. T. Colbert and W. H. Miller, J. Chem. Phys. **96**, 1982 (1992).
[43] B. R. Johnson, J. Chem. Phys. **67**, 4086 (1977).
[44] R. Schinke, *Photodissociation Dynamics* (Cambridge University Press, Cambridge, 1993).
[45] W. C. Martin, R. Zalubas, and A. Musgrove, J. Phys. Chem. Ref. Data **19**, 821 (1990).
[46] Y. Mo, H. Katayanagi, M. C. Heaven, and T. Suzuki, Phys. Rev. Lett. **77**, 830 (1996).
[47] M. C. G. N. van Vroonhoven and G. C. Groenenboom, J. Chem. Phys. **116**, 1965 (2002).
[48] A. M. Coroiu, D. H. Parker, G. C. Groenenboom, J. Barr, I. T. Novalbos, and B. J. Whitaker, Eur. Phys. J. D **38**, 151 (2006).
[49] Y. Mo and T. Suzuki, J. Chem. Phys. **109**, 4691 (1998).
[50] X. Chu, A. Dalgarno, and G. C. Groenenboom, Phys. Rev. A **72**, 032703 (2005).
[51] J. J. C. Teixeira-Dias and A. J. C. Varandas, Mol. Phys. **25**, 1185 (1973).
[52] M. Medveď, P. W. Fowler, and J. M. Hutson, Mol. Phys. **98**, 453 (2000).
[53] D. Č. Radenović, A. J. A. van Roij, S.-M. Wu, J. J. ter Meulen, D. H. Parker, M. P. J. van der Loo, and G. C. Groenenboom (unpublished).
[54] D. R. Herschbach, Faraday Discuss. Chem. Soc. **84**, 465 (1987).
[55] T. P. Rakitzis, P. C. Samartzis, and T. N. Kitsopoulos, Phys. Rev. Lett. **87**, 123001 (2001).